

# ZZ Studies and other stories

Nick Edwards

April 2013

# Contents

<b>I Background</b>	<b>2</b>
<b>1 Theory</b>	<b>3</b>
1.1 The Standard Model . . . . .	3
1.1.1 Fundamental Forces . . . . .	4
1.1.2 Fundamental Particle . . . . .	4
1.1.3 The Electroweak Force . . . . .	4
1.1.4 Electro-weak Symmetry breaking . . . . .	4
1.2 Monte-Carlo Simulations . . . . .	4
<b>2 ZZ Production</b>	<b>5</b>
2.1 Introduction . . . . .	5
2.2 Standard Model ZZ Production . . . . .	5
2.2.1 Feynman Diagrams . . . . .	5
2.2.2 Fiducial Volume Defintion . . . . .	5
2.2.3 Cross Section . . . . .	5
2.2.4 Generator level distributions . . . . .	5
2.3 Anomolous Triple Gauge Couplings . . . . .	5
2.4 ZZ Resonances . . . . .	5

<b>II Experimental Description</b>	<b>6</b>
<b>3 The ATLAS Detector at the LHC</b>	<b>7</b>
3.1 The Large Hadron Collider . . . . .	7
3.1.1 Machine Design . . . . .	7
3.1.2 Current Status . . . . .	9
3.2 The ATLAS Detector . . . . .	10
3.2.1 ATLAS Co-ordinate System . . . . .	13
3.2.2 Inner Detector . . . . .	13
3.2.3 Calorimetery . . . . .	18
3.2.4 Forward Calorimeter . . . . .	23
3.2.5 Muon Spectrometer (MS) . . . . .	23
3.3 Trigger and Data Aquisition . . . . .	25
3.4 Detector Simulation . . . . .	25
3.5 Experiment Performance and Data Samples . . . . .	25
<b>4 ATLAS Semiconductor Tracker Temperature Monitoring</b>	<b>26</b>
4.1 Introduction . . . . .	26
4.1.1 Effects of Radiation Damage on Semiconductor detectors . .	27
4.1.2 The Inner Detector Cooling System . . . . .	28
4.2 Methodology . . . . .	29
4.3 Monitoring Variables . . . . .	30
4.3.1 Front-Back temperature difference - $\Delta T$ . . . . .	30
4.3.2 Module temperature variation - $T_{\text{diff}}$ . . . . .	33
4.4 Time Evolution of monitoring variables . . . . .	39
4.4.1 Number of Problem modules . . . . .	39

4.5	Behaviour of problematic modules . . . . .	40
4.6	Conclusions . . . . .	42
<b>5</b>	<b>Object Reconstruction</b>	<b>43</b>
 <b>III Analysis</b>		<b>44</b>
<b>6</b>	<b>Object and Event Selection</b>	<b>45</b>
<b>7</b>	<b>Background Estimate</b>	<b>46</b>
<b>8</b>	<b>CrossSection</b>	<b>47</b>
8.1	Cross Section Definition . . . . .	47
8.2	Acceptances . . . . .	47
8.3	Systematic Uncertainties . . . . .	47
8.4	Cross Section Extraction . . . . .	47
<b>9</b>	<b>TGCLimits</b>	<b>48</b>
<b>10</b>	<b>Exotics</b>	<b>49</b>
<b>11</b>	<b>Conclusions</b>	<b>50</b>

# List of Figures

3.1	Cut-away view of the ATLAS detector [1]. The various detector sub-systems are labelled. . . . .	12
3.2	Cut-away view of the Inner Detector, taken from [2]. . . . .	14
3.3	Plan view of a quarter section of the Inner Dector showing the positions and pseudo-rapidity coverage of the various subdetectors. Figure taken from [2]. . . . .	15
3.4	Photograph of an SCT barrel module. . . . .	17
3.5	Cut-away view of the ATLAS calorimeter system. Image taken from [3]. . . . .	20
3.6	Diagram of the ATLAS liquid argon calorimeter, showing the accordian structure and the different granularity in the different layers. Diagram taken from [3]. . . . .	22
3.7	Cut away view showing the various components of the ATLAS muon spectrometer. Figure taken from [3]. . . . .	24
4.1	$\Delta T$ distribution for all SCT barrels averaged over the period 01:20 22/9/2012 to 01:20 23/9/2012. The distribution is fit to a Gaussian; the mean and width of the Gaussian is indicated on the plot. . . . .	31

4.2	$\Delta T$ distributions for the SCT Barrel 3 (a), Barrel 4 (b), Barrel 5 (c) and Barrel 6 (d) for 01:20 22/9/2012 to 01:20 23/9/2012. The distributions are fit to a Gaussian; the mean and width of the Gaussian is indicated on the plot. . . . .	32
4.3	$T_{\text{diff}}$ distributions for the SCT barrel and endcaps for 01:20 22/9/2012 to 01:20 23/9/2012 . . . . .	35
4.4	Problem modules on barrel 5 in April 2010 . . . . .	39
4.5	The number of ‘problematic’ modules with (a) $\Delta T$ and (b) $T_{\text{diff}}$ of greater magnitude than the problem threshold per day as a function of time between 20/01/2010 to 16/10/2012. The number of ‘problematic’ modules is not seen to increase significantly as a function of time. . . . .	40
4.6	The temperature difference between the front and back of the module ( $\Delta T$ ) for barrel module Q3/B6/L126/I/P29/A5 (left) and barrel module Q3/B6/L126/O/P30/C6 (right) as a function of time between 20/1/2010 to 18/7/2010 . . . . .	41
4.7	The difference in temperature between the module and its neighbours ( $T_{\text{diff}}$ ) as a function of time for module Q2/B5/L102/I/P24/C3 (left) Q4/ECA/D4/L160/RO/07 (right) between 20/1/2010 to 18/7/2010. . . . .	42

# List of Tables

3.1	LHC operational parameters. A comparison is made of the nominal design parameters [4], and those used in 2011 operation and in 2012 operation [5] [6]. . . . .	9
3.2	Performance goals of the ATLAS detector. Units of $p_T$ and $E$ are GeV. . . . .	11
4.1	The width, goodness of fit and mean of the Gaussian fit to the $\Delta T$ distribution averaged over stable periods between 20/1/2010 and 20/6/2010. . . . .	33
4.2	Number and percentage of modules with $ \Delta T $ greater than the threshold for identifying problem modules at least 5 times during the period 20/1/2010 - 19/6/2010 for each barrel. . . . .	34
4.3	The rms width of a Gaussian fit to the $T_{\text{diff}}$ distribution for each stable period between 20/1/2010 and 20/6/2010. The threshold used for identifying high $T_{\text{diff}}$ modules is set as 5 times this value; this is also shown in the second column. The third column shows the $\chi^2$ goodness of fit parameter. . . . .	37



# Acknowledgements

## **Abstract**

Four leptons blah blah

# **Introduction**

# **Part I**

## **Background**

# Chapter 1

## Theory

### 1.1 The Standard Model

The Standard Model of particle physics is a gauge theory describing the fundamental components of matter and their interactions, and encompasses our current understanding of the world at particle level. The Standard Model was formulated in the 1970s, and since then has been tested to an unprecedented level of precision. This section describes the particle content and the fundamental forces of the Standard Model.

**1.1.1 Fundamental Forces**

**1.1.2 Fundamental Particle**

**1.1.3 The Electroweak Force**

**1.1.4 Electro-weak Symmetry breaking**

**1.2 Monte-Carlo Simulations**

# **Chapter 2**

## **ZZ Production**

### **2.1 Introduction**

### **2.2 Standard Model ZZ Production**

#### **2.2.1 Feynman Diagrams**

#### **2.2.2 Fiducial Volume Defintion**

#### **2.2.3 Cross Section**

#### **2.2.4 Generator level distributions**

### **2.3 Anomolous Triple Gauge Couplings**

### **2.4 ZZ Resonances**

# **Part II**

# **Experimental Description**

# Chapter 3

## The ATLAS Detector at the LHC

### 3.1 The Large Hadron Collider

The Large Hadron Collider (LHC) is a particle accelerator located at CERN, the European Organisation for Nuclear Research, on the French-Swiss border near Geneva. The LHC is the world's most powerful accelerator, colliding beams of protons together at centre of mass energies of up to 8 TeV, with the aim of better understanding the workings of our Universe. It is installed in tunnel of circumference 26.7 km, which previously held the Large Electron-Positron Collider (LEP), and is between 45 and 170 m below the ground. It is also capable of colliding heavy ions, providing a complimentary heavy-ion physics program.

#### 3.1.1 Machine Design

The LHC consists of two counter-circulating beams of protons. Dipole magnets are used to bend the beams and keep them in orbit. Quadrupole magnets are used to keep the beams focussed. Since the beams are of similarly charged particles

orbiting in opposite directions, they require opposite bending fields, thus need to be in separate beampipe. Due to space constraints, the two beams are contained within a single structure incorporating a twin bore superconducting magnet. The magnets must be cooled to 2K to retain their superconducting properties; this is achieved with a helium based cooling system.

Protons are injected into the LHC from the SPS (Super Proton Synchrotron) in bunches, at a centre of mass energy of 450 GeV. They are then accelerated to the desired collision energy by means of superconducting Radio Frequency (RF) cavities. Once the particles are accelerated to full energy, the RF cavities are used to keep the particles in their bunches. The bunches are brought to collision at four points around the ring, at each of which a different experiment is located. ATLAS sits at point 1, the ALICE experiment at Point 2, the CMS experiment at Point 5, and the LHCb experiment at Point 8 (the remaining ‘Points’ are access locations to the ring).

The rate at which collisions occur depends on the instantanious luminosity  $\mathcal{L}$  and the collision cross-section  $\sigma$ , related by:

$$\frac{dN}{dt} = \mathcal{L} \cdot \sigma \quad (3.1)$$

The total cross-section for proton-proton collisions at the LHC is ???. The rate at which a particular physics process occurs depends on the cross section for the process in question. Since many of the physics processes under study at the LHC are very rare and have small cross-sections, it is important to maximise the luminosity as much as possible. The instantaneous luminosity can be maximised by increasing the number of particles per bunch, decreasing the bunch spacing (or

equivalently increasing the number of bunches per beam) or decreasing the size of the bunch at the interaction point.

A measure of how many collisions have occurred is the integrated luminosity:

$$L = \int \mathcal{L} dt \quad (3.2)$$

The number of events occurring for a given process with cross-section  $\sigma_{\text{process}}$  is given by:

$$N_{\text{process}} = L \cdot \sigma_{\text{process}} \quad (3.3)$$

### 3.1.2 Current Status

The LHC began operation in November 2009 with collisions at a centre of mass energy of 900 GeV, with the centre of mass energy raising to a world record 2.36 TeV by the end of the year. In 2010 the centre of mass energy was successfully increased to 7 TeV.

Details of the LHC operational parameters in 2011 and 2012, together with the nominal design values, are given in Table 3.1.

Parameter	Design	2011 Operation	2012 Operation
Proton Energy	7 TeV	3.5 TeV	4 TeV
No. particles per bunch (max)	$1.15 \times 10^{11}$	$1.5 \times 10^{11}$	$1.6 \times 10^{11}$
No. of bunches per beam (max)	2808	1380	1380
Bunch spacing	25 ns	50 ns	50 ns
Peak Luminosity (max)	$1.0 \times 10^{34} \text{cm}^{-2}\text{s}^{-1}$	$3.6 \times 10^{33} \text{cm}^{-2}\text{s}^{-1}$	$7.7 \times 10^{33} \text{cm}^{-2}\text{s}^{-1}$

Table 3.1: LHC operational parameters. A comparison is made of the nominal design parameters [4], and those used in 2011 operation and in 2012 operation [5] [6].

## 3.2 The ATLAS Detector

ATLAS (A Toroidal LHC ApparatuS) is one of two general purpose particle-physics detectors at the LHC, built to study both particle-particle and ion-ion interactions. The high centre of mass energy and high luminosity of LHC proton-proton collisions allows the study of physics at the TeVscale for the first time, as well as precision measurements of the Standard Model. ATLAS has been designed to be capable of a wide range of measurements, including (but by no means limited to) high precision tests of QCD, electroweak interactions, and flavour physics, searching for and measuring the properties of the Higgs Boson, searches for supersymmetry, measurements of the properties of the top-quark, searches for new vector bosons and searches for extra-dimensions. The extremely high luminosity also presents challenges which the detector has been designed to overcome. At design luminosity,  $10^9$  inelastic collisions occur per second, which results in multiple events, on average ?? in 2012 running, occurring simultaneously. The detector has been designed to cope with these high ‘pile-up’ conditions, as well as be capable of operating in the high radiation environment arising from the high luminosity. Many of the physics processes of interest occur at very small rates with respect to extremely high QCD background rates. The detector must therefore allow processes of interest to be distinguished from the background. To meet these challenges, ATLAS was defined with the following criteria in mind:

- Fast, radiation hard electronics and sensors.
- High granularity to cope with high particle fluxes and overlapping events.
- Full azimuthal coverage to allow for missing transverse energy measurement,

and large acceptance in pseudo-rapidity.

- Precision tracking to provide good charged particle momentum resolution and reconstruction efficiency, and to allow observation of secondary vertices to identify  $b$ -hadrons and  $\tau$ -leptons.
- Excellent electromagnetic calorimetry for electron and photon identification.
- Full-coverage hadronic calorimetry for accurate jet and missing transverse energy measurements.
- Good muon identification, momentum resolution and charge determination over a wide range of momentum.
- Efficient triggering on low transverse-momentum object with sufficient background rejection.

The main performance goals are given in Table 3.2.

Detector Component	Required Resolution	$\eta$ coverage	
		Measurement	Trigger
Tracking	$\sigma_{p_T}/p_T = 0.05\% p_T \oplus 1\%$	$\pm 2.5$	None
EM Calorimetry	$\sigma_E/E = 10\%/\sqrt{E} \oplus 0.7\%$	$\pm 3.2$	$\pm 2.5$
Hadronic Calorimetry			
Barrel and End-Cap	$\sigma_E/E = 50\%/\sqrt{E} \oplus 3\%$	$\pm 3.2$	$\pm 3.2$
Forward	$\sigma_E/E = 100\%/\sqrt{E} \oplus 10\%$	$3.1 <  \eta  < 4.9$	$3.1 <  \eta  < 4.9$
Muon Spectrometer	$\sigma_{p_T}/p_T = 10\% \text{ at } p_T = 1 \text{ TeV}$	$\pm 2.7$	$\pm 2.4$

Table 3.2: Performance goals of the ATLAS detector. Units of  $p_T$  and  $E$  are GeV.

A cut-away view of the ATLAS detector [3] is shown in Figure 3.1. The detector consists of an inner tracking detector, which is surrounded by electromagnetic and

hardonic calorimeters and finally a muon spectrometer. The inner detector is immersed in a 2 T solenoidal field to allow for momentum measurement. The muon spectrometer is also immersed in a magnetic field, provided by an air-core toroid system which generates strong bending power over a large volume with a minimum of material, thus minimising multiple-scattering effects. A three-level trigger system is used to select events to read out. These sub-systems are described in more detail in the following sections.

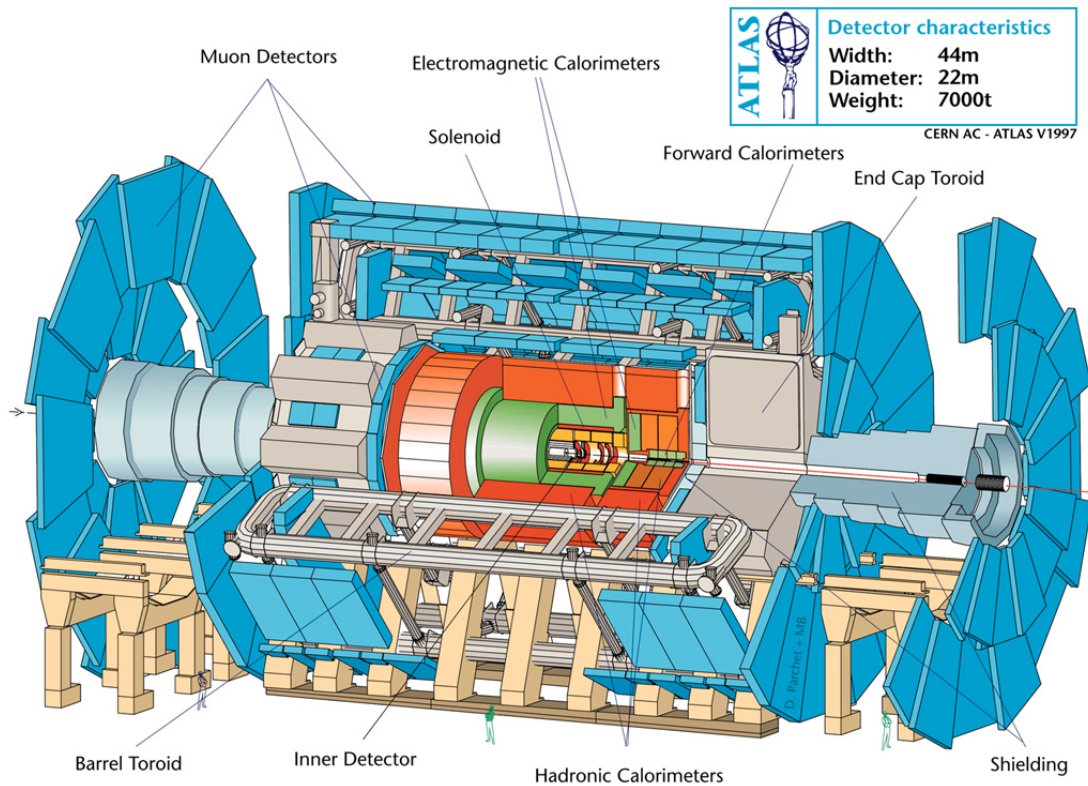


Figure 3.1: Cut-away view of the ATLAS detector [1]. The various detector sub-systems are labelled.

### 3.2.1 ATLAS Co-ordinate System

ATLAS uses a right-handed coordinate system with its origin at the nominal interaction point in the centre of the detector. The  $z$ -axis points along the beam-pipe, the  $x$ -axis towards the centre of the LHC ring, and the  $y$ -axis upwards. Particle directions and detector element positions are generally described by their azimuthal angle  $\phi$  and their pseudorapidity  $\eta$ . The azimuthal angle describes the angle in the  $x$ - $y$  plane, with  $\phi = 0$  along the  $x$ -axis, increasing clockwise around the beam-pipe. The pseudorapidity  $\eta$  is defined in terms of the polar angle  $\theta$  (the angle in the  $x - z$  plane) as  $\eta = -\ln \tan(\theta/2)$ , and is an approximation to rapidity in the high energy limit. The radial co-ordinate  $R$  measures the radial distance from the interaction point.

### 3.2.2 Inner Detector

The ATLAS Inner Detector (ID) is located closest to the beam pipe. It is a tracking detector designed to provide hermetic and robust pattern recognition, locate interaction vertices, including displaced secondary vertices from long-lived particles, and provide a precise measurement of the transverse momenta of charged particles with a nominal  $p_T$  threshold of 0.5 GeV. The Inner Detector consists of a silicon pixel detector (the “Pixel Detector”, a silicon strip detector (the “Semiconductor Tracker” or SCT) and a transition radiation tracker (the TRT), located within a 2 T magnetic field provided by a solenoidal superconducting magnet.

A cut-away diagram of the Inner Detector is shown in Figure 3.2. The detector is cylindrical in shape, extending 3512 mm either side of the interaction point in the  $z$  direction with a radius of 1150 mm. The subdetectors all consist of concentric

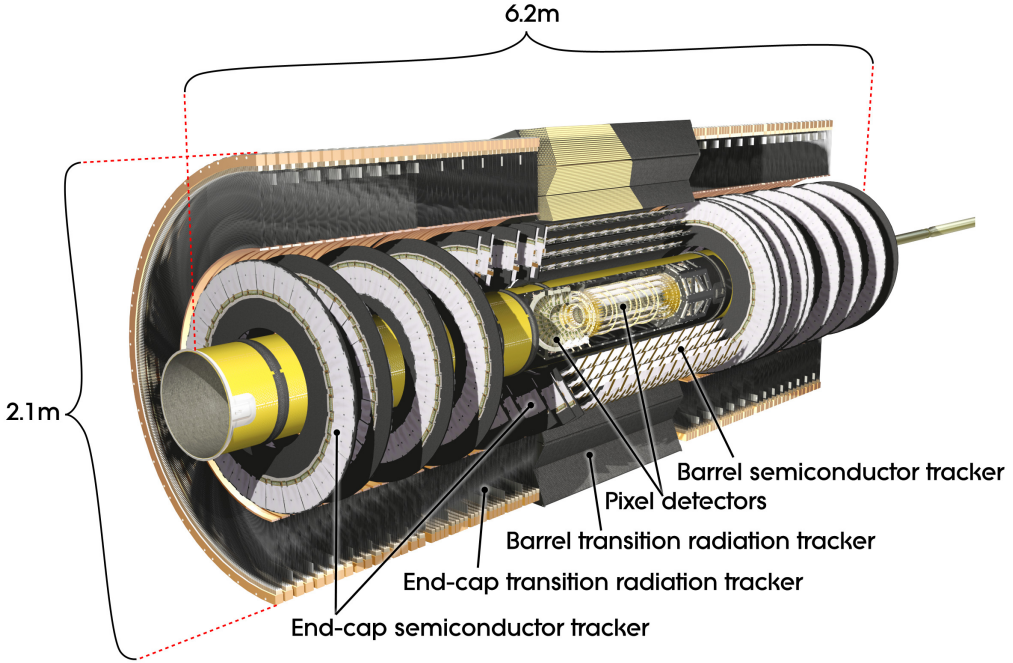


Figure 3.2: Cut-away view of the Inner Detector, taken from [2].

cylindrical layers surrounding the beam pipe, referred to as ‘barrels’, with disks referred to as ‘end caps’ covering each end of the barrels. A plan view of a quarter of the Inner Detector is shown in Figure 3.3. The Pixel and SCT detectors provide coverage up to  $|\eta| < 2.5$ , with the TRT enhancing pattern recognition and track momentum resolution up to  $|\eta| < 2.0$

## Pixel Detector

The pixel detector is the detector component closest to the beam. It is formed of layers of silicon semiconducting pixels, and is designed to have a very high granularity for resolving primary and secondary interaction vertices. There are three barrel layers closed by an endcap consisting of three disks at each end. The barrels are numbered from 0 to 2. The closest layer to the beam pipe, termed the

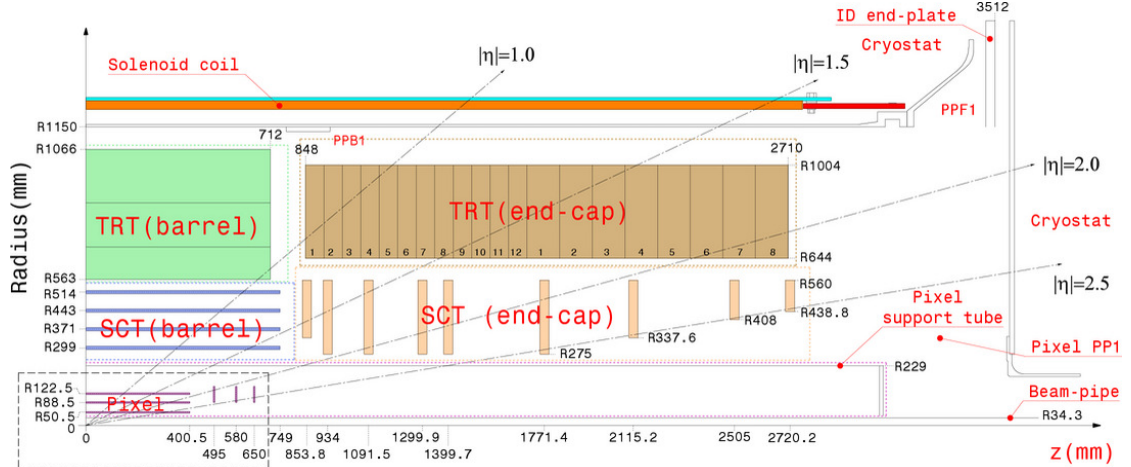


Figure 3.3: Plan view of a quarter section of the Inner Detector showing the positions and pseudo-rapidity coverage of the various subdetectors. Figure taken from [2].

$b$ -layer (due to it's important role in detecting secondary vertices for  $b$  physics), is positioned at a radius of 50.5 mm. Due to the high radiation dose that it will receive at this position, it will need to be replaced after three years operation at design luminosity.

The detector layers are formed of sensor modules. Each module consists of a 250  $\mu\text{m}$  thick silicon sensor consisting of 46,080 active pixels. There are a total of 1,744 modules, all with identical dimensions of  $19 \times 400 \mu\text{m}^2$ . In total there are approximately  $80.4 \times 10^6$  readout channels.

Typically particles will traverse three layers of the detector, in most case producing three space-points. The intrinsic accuracy of the position measurement is 10  $\mu\text{m}$  in  $(R - \phi)$  and 155  $\mu\text{m}$  in  $z$  in the barrel layers and 10  $\mu\text{m}$  in  $(R - \phi)$  and 155  $\mu\text{m}$  in  $\phi$  in the endcaps.

## Semiconductor Tracker (SCT)

The SCT is a silicon strip detector, consisting of four barrels and two end-caps consisting of nine disks each. The barrels consist of 2112 separate modules and extend from a radius of 299 mm from the beam line at the innermost barrel to a radius of 514 mm at the outermost. The barrels are numbered from 3 to 6. Each endcap consists of 988 modules, arranged in such a way that a particle must pass through four layers of the detector.

SCT modules are made from two layers of single sided p-in-n silicon chips biased at 150V (this voltage will increase as the detector become radiation damaged). Charged particles passing through the depletion region at the centre of the junction produce electron hole pairs, which are swept apart by the bias voltage. The electrons are then collected on the top of the chip, producing a signal which can be read out. A photo of an SCT barrel module is shown in Figure 3.4.

Each side of the module consists of 768 strips, with a pitch of  $80 \mu\text{m}$  for barrel modules, and an average pitch of  $80 \mu\text{m}$  for endcap modules. The strips are 6.4 cm long, and run parallel to the beam axis on the barrel, and along the  $R$  direction on the endcap. In total there are approximately  $6.3 \times 10^6$  readout channels.

The two layers are glued together at a stereo angle of 40 mrad to form a two sided module. The readout is of a binary form, with a charge collection threshold of 1 fC (chosen to maximise efficiency and minimise noise). To form a space-point, a coincidence of hits on either side of the module is required. The stereo angle gives the ability to determine where along the strip the hit occurred, giving resolution in  $z$  ( $R$ ) in the barrels (endcaps). A small angle is used to prevent ambiguities in the presence of multiple nearby hits. The spatial resolution of the detector is  $17 \mu\text{m}$ .

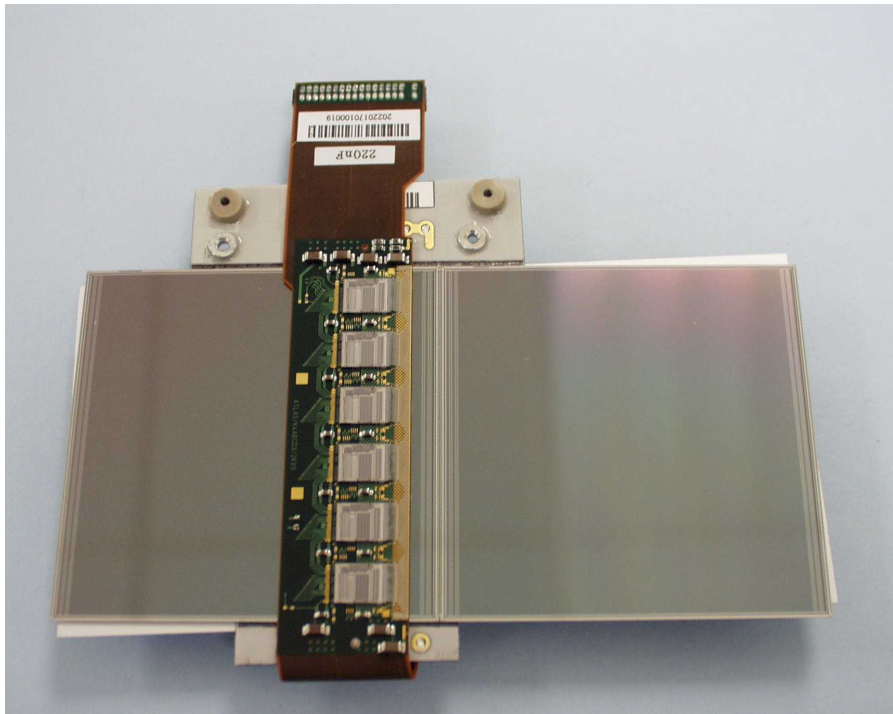


Figure 3.4: Photograph of an SCT barrel module.

in  $(R - \phi)$  and  $580 \mu\text{m}$  in  $z$  (in the barrel) or  $R$  (in the endcaps).

### Transition Radiation Tracker (TRT)

The Transition Radiation Tracker is a straw drift tube tracker, with additional particle identification capabilities from transition radiation. It consists of modules formed from bundles of 4 mm diameter straws, filled with  $\text{XeCO}_2\text{O}_2$  gas. A tungsten wire of  $30 \mu\text{m}$  diameter runs down the centre of the tube to collect charge. In the barrel the straws run parallel with the beam axis and are 144 cm long. The wires are electrically divided into two halves at  $|\eta| = 0$  and read out at either end (this subdivision leads to an inefficiency along a length of approximately 2 cm at the centre of the TRT). In the endcaps the straws are 37 cm long and run radially. In total there are 351,000 readout channels.

All charged tracks with  $p_T > 0.5$  GeV and  $|\eta| < 0.2$  will traverse at least 36 straws, except in the barrel to endcap transition region ( $0.8 < |\eta| < 1.0$ ) where only 22 straws will be traversed. The  $(R - \phi)$  resolution is  $130\text{ }\mu\text{m}$ . Despite the low resolution compared to the silicon trackers, and the lack of a measurement in the  $z$  direction, the hits in the TRT contribute significantly to the pattern recognition and momentum resolution due to the large number of measurements and longer measured track length.

The barrel straws are embedded in a matrix of  $19\text{ }\mu\text{m}$  diameter polypropylene fibres, and the endcap disk layers are sandwiched between  $15\text{ }\mu\text{m}$  polypropylene foils. When charged particles cross these boundaries they emit transition radiation photons. These photons are then absorbed in the Xenon gas mixture, and produce much larger signals than minimum-ionising charged particles. The energy of the transition radiation photons depends heavily on particle type, and is approximately 200 keV for a 20 GeV electron and 1 keV for a 20 GeV pion. This difference can be exploited for particle identification, by counting the number of hits over a higher threshold. Electrons with  $p_T > 2$  GeV typically produce 7 - 10 high threshold hits, whereas pions and other charged particles will produce far fewer.

### 3.2.3 Calorimetry

Sitting outside the inner detector and its magnetic field are the ATLAS calorimeter systems. The purpose of the calorimeter is to measure the energy and position of particles. A particle entering the calorimeter will produce a ‘shower’ of secondary particles. The energy of this shower is then measured. ATLAS uses sampling calorimeter, in which different materials, sandwiched together in layers, are used

for the absorption and the energy measurement. This allows for a more compact design and hence better shower containment. Position measurement is obtained by segmenting the calorimeter in the  $z$  and  $\phi$  directions.

Different absorbers are required depending on whether the particle interacts electromagnetically or strongly, and the properties of the showers that develop are different. The ATLAS calorimeters are divided into two distinct subsystems, the Electromagnetic calorimeter and the Hadronic calorimeter. An Electromagnetic shower consists of electrons and photons, and is normally fully contained in the calorimeter; thus it can be fully detected. Hadronic showers involve many more particle types, including muons and neutrinos which escape detection, and tend to be longer and wider, often spilling out of the calorimeter. The full energy of the shower is thus not fully detected, and so a calibration of the energy response is required. It is important for the calorimeter to provide good containment for electromagnetic and hadronic showers, not only for the purposes of energy measurement, but also to allow a good missing transverse energy requirement, and to prevent punch-through into the muon system.

A cutaway view showing the location of the various calorimeter elements is shown in Figure 3.5. The calorimeters cover the range  $|\eta| < 4.9$ . Over the  $\eta$  range of the inner-detector, the Electromagnetic calorimeter gives fine granularity to allow precise measurement of electrons and photons. The Hadronic calorimeter is more coarsely segmented, but is sufficient to meet the requirements of jet and missing transverse energy measurement.

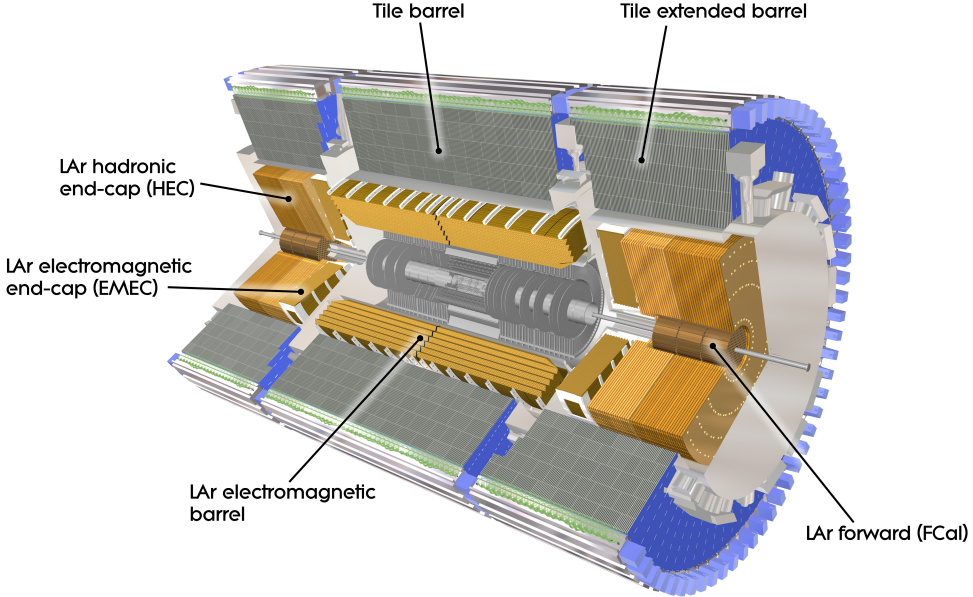


Figure 3.5: Cut-away view of the ATLAS calorimeter system. Image taken from [3].

### Electromagnetic Calorimeters

The electromagnetic calorimeter (also referred to as the *LAr*) uses liquid argon as the active detector material, and lead as an absorber. Incident particles ionise atoms in the lead absorber, creating an electromagnetic shower. Charged particles in the shower ionise the liquid argon, where the electrons drift to copper electrodes in the presence of an electric field.

The calorimeter consists of two half barrels extending to  $|\eta| < 1.475$  (with a 4 mm gap at  $z = 0$ ) and two coaxial wheels on each side, the first covering  $1.375 < |\eta| < 2.5$  and the second covering  $2.5 < |\eta| < 3.2$ . Additional material needed to instrument and cool the detector creates a ‘crack’ region at  $1.375 < |\eta| < 1.52$ , where the energy resolution is significantly degraded.

The barrel calorimeter has an accordian structure in order to avoid azimuthal

cracks and to provide full  $\phi$  symmetry, as shown in figure Figure 3.6. The accordion structure is made of the lead absorber, with the liquid argon filling the 2.11 mm gaps between the absorbers. The barrel of the LAr calorimeter is divided into three layers, with different cell granularity. The first layer is divided into cells of  $\Delta\eta \times \Delta\phi = 0.0031 \times 0.098$ . The fine granularity in  $\eta$  of this layer is used to determine the pseudo-rapidity of the particle, and for measurements of the shower shape, an important input to particle identification. The second layer has cell size  $\Delta\eta \times \Delta\phi = 0.0245 \times 0.025$  and contains the largest energy fraction of the shower, measuring approximately 16 radiation lengths. The third layer, with cell size  $\Delta\eta \times \Delta\phi = 0.0245 \times 0.05$ , collects the tail of the shower. The first wheel of the LAr calorimeter is also segmented into three layers with the same granularity as the barrel. The second wheel has a coarser granularity that varies as a function of pseudorapidity. A liquid argon presampler exists for  $|\eta| < 1.8$  to correct for energy lost by incident particles traversing material before the calorimeters.

## Hadronic Calorimeters

The hadronic calorimeter consists of a plastic scintillator tile calorimeter (referred to as the *Tile* calorimeter) covering  $|\eta| < 1.7$  and a liquid argon endcap calorimeter (referred to as the *HEC*) covering  $1.5 < |\eta| < 3.2$ .

The tile calorimeter consists of a 5.8 m long barrel covering  $|\eta| < 0.8$  and two 2.6 m long extended barrels covering  $0.8 < |\eta| < 1.7$ . It is located immediately behind the EM calorimeter, extending from a radius of 2.28 m to a radius of 4.25 m. The active material consists of 3 mm thick layers of the plastic scintillator placed perpendicular to the beam direction, sandwiched between a steel absorber. The scintillators are connected at each end to readout photomultipliers

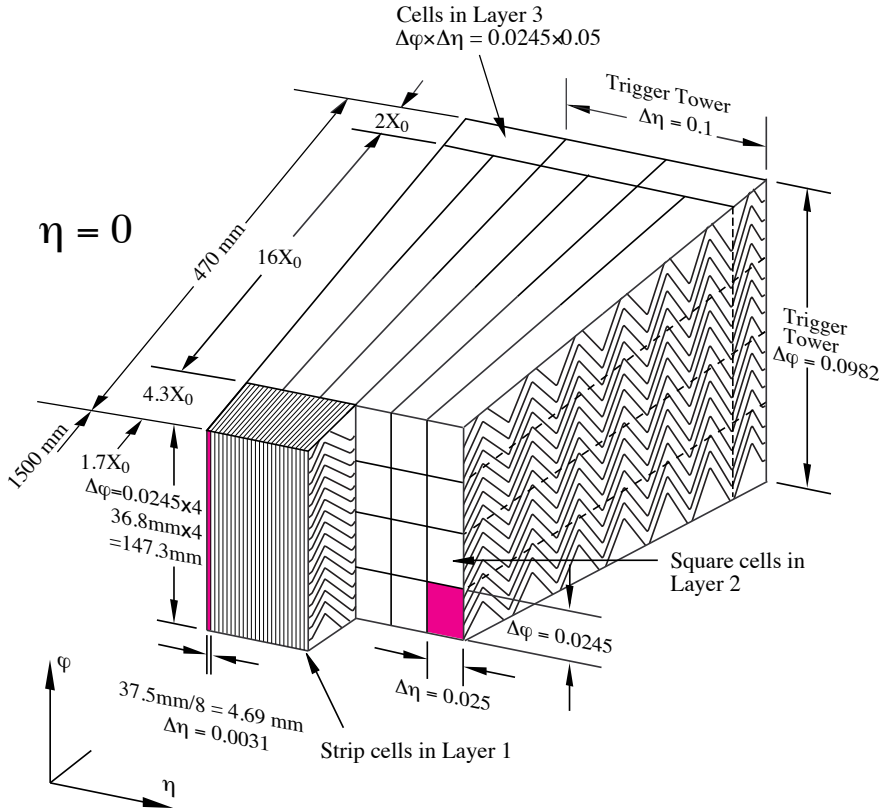


Figure 3.6: Diagram of the ATLAS liquid argon calorimeter, showing the accordian structure and the different granularity in the different layers. Diagram taken from [3].

by wavelength shifting fibres. The fibres are grouped together to form readout cells, giving projective towers in  $\eta$ . There are three layers of cells, with a granularity of  $\Delta\eta \times \Delta\phi = 0.1 \times 0.1$  in the first two layers, and  $\Delta\eta \times \Delta\phi = 0.1 \times 0.2$  in the third.

The HEC consists of two wheels per endcap, HEC1 and HEC2, located directly behind the EMEC and sharing the same cryostat. Each wheel has two layers of cells. The HEC covers  $1.5 < |\eta| < 3.2$  and so overlaps with the Tile calorimeter on one side and the FCAL on the other, thus avoiding cracks in the transition regions.

HEC1 (HEC2) is built from 25 mm (50 mm) copper plate absorbers interleaved with 8.5 mm gaps containing liquid argon. The liquid argon gaps are split into four drift spaces of roughly 1.8 mm by three electrodes. This is to avoid ion-build up due to the higher particles fluxes and energies in the forward region, and also allows a lower high voltage than a single electrode design.

### 3.2.4 Forward Calorimeter

The forward calorimeter (*FCAL*) covers  $3.1 < |\eta| < 4.9$ . To reduce the netron flux, the FCAL begins 1.2 m away from the Electromagnetic calorimeter front face. Due to the high particle fluxes and energies in the forward region, the calorimeter must contain relatively long showers in the small volume allowed by design constraints, and thus must be very dense. The FCAL is divided into thre compartments. The first, FCAL1, is designed for electromagnetic measurements, and uses copper as an active material with liquid argon as a passive material. The second two compartments, FCAL2 and FCAL3, are designed for hadronic measurements, and use tungsten as a passive material, chosen for it's high density to provide containment and minimise the lateral spread of hadronic showers. An additional copper alloy shielding plate is places behind FCAL3 to reduce background to the muon endcap system.

### 3.2.5 Muon Spectrometer (MS)

The muon spectrometer sits outside of the calorimeter system. It is designed to provide precision muon momentum measurements over a momentum range of 3 GeV to 3 TeV, as well as providing triggering on interesting bunch crossings

containing muons. An overview of the MS is given in Figure 3.7. The system sits inside a giant air coil toroidal magnet system, producing a magnetic field orthogonal to the muon momentum to provide deflection of the muons for momentum measurement. The use of an air coil reduces multiple scattering which degrades the momentum resolution.

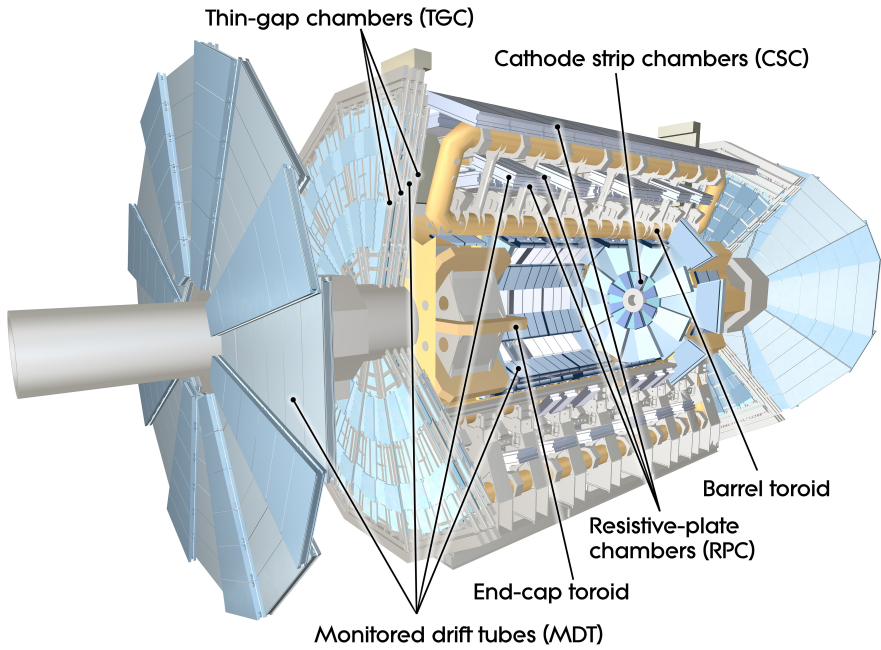


Figure 3.7: Cut away view showing the various components of the ATLAS muon spectrometer. Figure taken from [3].

The system consists of Monitored Drift Tubes (MDT) and Cathode Strip Chambers (CSC) to provide precision measurements in the bending ( $y - z$ ) plane. The MDT covers  $|\eta| < 2.7$  and consist of three layers. The mechanical isolation of the sensor wire in each tube from it's neighbours give a reliable system design. In the innermost layer, for  $2.0 < |\eta| < 2.7$  the MDT is replaced by the CSC due to the higher rates and higher backgrounds in this region. The CSC is a multiwire proportional chamber, and so gives a higher granularity than the MDT and is

better able to cope with high rates and fluxes.

Resistive Plate Chambers (RPC) and Thin Gap Chambers (TGC) provide triggering for  $|\eta| < 2.4$  and a measurement in the  $x - y$  plane for  $|\eta| < 2.7$ . The RPC covers  $|\eta| < 1.05$ , with the TGC covering  $1.05 < |\eta| < 2.7$ . The muon trigger has a time resolution of between 1.5 ns and 4 ns.

### **3.3 Trigger and Data Aquisition**

### **3.4 Detector Simulation**

### **3.5 Experiment Performance and Data Samples**

# Chapter 4

## ATLAS Semiconductor Tracker Temperature Monitoring

### 4.1 Introduction

In order to mitigate the effects of radiation damage, it is necessary to maintain the SCT modules at a temperature of around  $-7^{\circ}\text{C}$ . The SCT and Pixel sub-detectors use a common evaporative cooling system to keep their silicon structures at the required temperatures. In order to monitor the performance of the cooling of SCT modules, the temperature of each module is monitored by a thermistor mounted on the front side of the detector (the side furthest from the interaction point). The barrel modules have an additional thermistor mounted on the back side of the module. Monitoring of the module temperature is important to ensure that the cooling system is functioning as designed and that the modules are still coupled to the cooling structures. The temperature difference between the front and the back of barrel modules can be used to identify modules losing mechanical

integrity. To this end tools were developed to monitor variables associated with the temperatures of SCT modules. These are described in this section, along with results for twenty-two months of operation between January 2010 and October 2012.

#### 4.1.1 Effects of Radiation Damage on Semiconductor detectors

Given the LHC design luminosity of  $10^{34}\text{cm}^{-2}\text{s}^{-1}$ , the inner layers of the SCT are expected to receive a radiation dose of up to  $2 \times 10^{14}\text{n}_{\text{eq}}/\text{cm}^2$  [7] over the course of it's design lifetime of 10 years. Exposure to such high radiation doses causes damage to the silicon detectors.

The primary cause of damage is interactions with irradiating particles displacing nuclei from their lattice position. This can have the effect of removing donors, or of creating acceptor like defects. Exposure to radiation will eventually cause an n-type semi-conductor to become less heavily doped, and in extreme causes change the material from n-type to p-type. Consequently, the displacement voltage required to fully deplete the detector increases, and for sufficiently high radiation doses it becomes impossible to fully deplete the detector. It is therefore essential to reduce the effects of radiation damage as much as possible.

The effects of exposure to radiation have both an immediate and a prolonged effect. Immediate effects include the removal of donor nuclei from the lattices, and creation of acceptor like defects. Due to the complicated kinetics of these defects after the radiation, an annealing effect occurs which initially reduces the number of acceptor-like defects, on a timescale of approximately two days, but on a longer

term a ‘reverse annealing’ occurs, increasing the number of acceptors. The rate of the reverse annealing effect is dependant on the temperate of the silicon. It is found that for temperatures of approximately -7°C the reverse-annealing effect is effectively frozen out [8]. Since the reverse annealing occurs even after radiation, it is important to run the detector cooling at all times, not just when particle collisions are occurring.

Lattice defects introduced as a result of exposure to radiation also causes an increase of the leakage current, and a loss of mobility, both of which increases the level of noise in the detector. Since the leakage current is induced by thermal creation of electron-hole pairs from shallow donors, the size of the leakage current is also dependant on temperature:

$$I_{\text{leakage}}(T) \propto T^2 e^{-\frac{E_g}{2k_B T}} \quad (4.1)$$

#### 4.1.2 The Inner Detector Cooling System

As described in the previous section, the SCT silicon detectors must be run at temperatures of around -7°C in order to slow the rate of radiation damage and prolong their lifetime. Each SCT module currently produces between 5.5W and 6W of heat when the “High Voltage (HV)” biasing voltage is applied. This is expected to increase to around 8W as the detector suffers the effects of radiation damage and the bias voltage must be increased to compensate.

An active cooling system based upon evaporative cooling is used to cool the SCT and Pixel modules [9]. An evaporative cooling system was chosen over a mono-phase system as it has a larger cooling capacity per unit volume due to

utilisation of the latent heat of vaporisation rather than a liquid’s heat capacity. This allows the resulting system to be smaller and with a lower mass, thus resulting in less material in the inner-detector. Additionally, an evaporative system has smaller temperature gradients along long cooling tubes, allowing for more uniform module temperatures.

The system uses  $C_3F_8$  gas, delivered at room temperatures to capillaries located immediately before the detector structure. The fluid expands through the capillaries and passes along a cooling pipe at boiling point. The modules are coupled to the pipe by means of cooling blocks and heat is absorbed from the modules by the passing fluid causing it to evaporate. The exhaust gas is then compressed, condensed, and returned to the cooling loop.

The system consists of 204 independent cooling circuits or ‘loops’. 44 of these cool modules on the SCT barrels, 72 cool modules on the SCT endcaps and the remaining 88 cool modules on the Pixel detector.

## 4.2 Methodology

The temperatures recorded by the module thermistors are read out by the ATLAS *PVSS* SCADA system. Twice a day the temperatures are written to an Oracle database for offline analysis. In addition, whenever a module temperature changes above a deadband of  $0.4^\circ C$  the new value is written to the database. It is necessary to first find periods of stable running where the cooling system is turned on and the system in a stable state. Stable periods are found by requiring that the number of cooling loops turned on is constant and greater than zero. Stable periods are required to be at least 6 hours long, to veto periods where the detector is being

turned on and off. Stable periods longer than 24 hours are broken down into 24 hour blocks.

For each module, a number of monitoring variables are calculated; these are described below. The distributions of these variables are plotted for each of the barrel layers and endcap disks. Modules which fall in the far outlying regions of the distributions are identified as ‘problem’ modules. A list of problem modules is maintained, and these modules are monitored. The plots are produced automatically on a daily basis by scripts running on one of the SCT monitoring computers. The plots are made available as part of the ‘SCT Calibration Monitoring’ website at <https://pc-sct-www01.cern.ch/CalibMonitor/> (ATLAS login required).

## 4.3 Monitoring Variables

### 4.3.1 Front-Back temperature difference - $\Delta T$

SCT barrel modules have two thermistors, one mounted on either side of the module. The difference in temperature between the front and back of the module should be very small and any large temperature difference would indicate defective thermal coupling between the two sides. This would suggest that the front and the back of the module had lost mechanical integrity and were coming apart from one another. The monitoring variable  $\Delta T$  is defined as

$$\Delta T = T_{\text{front}} - T_{\text{back}} \quad (4.2)$$

where  $T_{\text{front}}$  and  $T_{\text{back}}$  are the temperatures recorded at the front and the back of the module respectively.

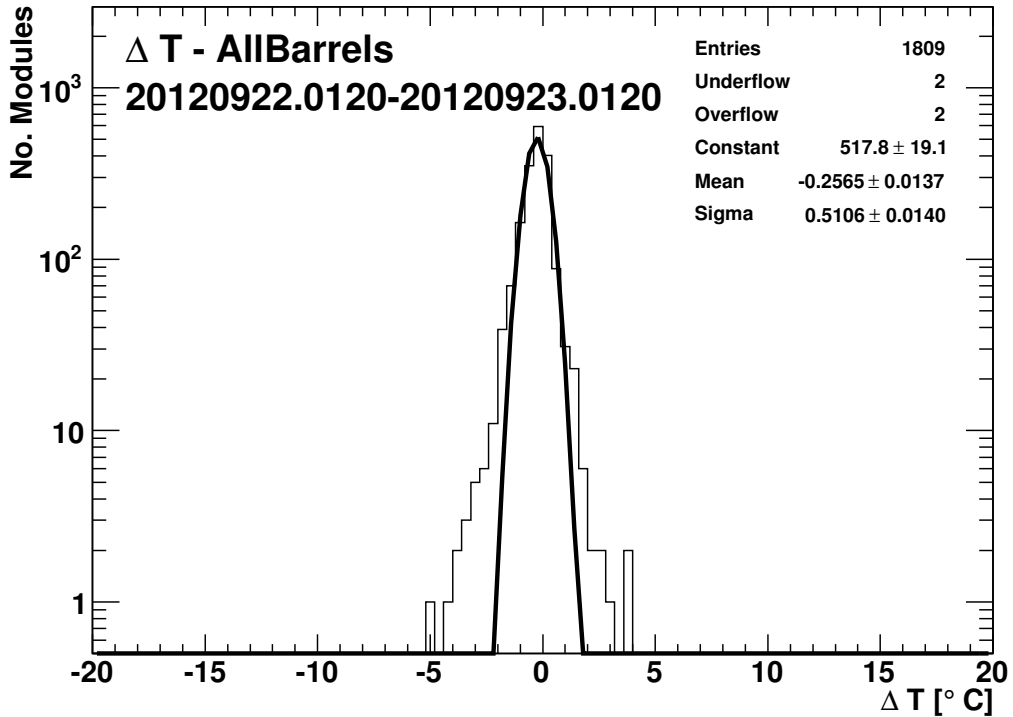


Figure 4.1:  $\Delta T$  distribution for all SCT barrels averaged over the period 01:20 22/9/2012 to 01:20 23/9/2012. The distribution is fit to a Gaussian; the mean and width of the Gaussian is indicated on the plot.

For each period of stable operation the distribution of  $\Delta T$  is plotted, for all barrels together as well as for each barrel separately. Example plots for 01:20 22/9/2012 to 01:20 23/9/2012 are shown in Figure 4.1 (all barrels) and in Figure 4.2 (separately for each barrel). The distributions are fitted with a Gaussian and the mean and width of the Gaussian are obtained. These are listed in Table 4.1 for each of the barrel layers, averaged over 5 months of data between 20/1/2010 and 20/6/2010.

In order to identify modules with a high value of  $\Delta T$ , a threshold of 5 times the width of the Gaussian is set, separately for each barrel. Modules with a value of  $\Delta T$

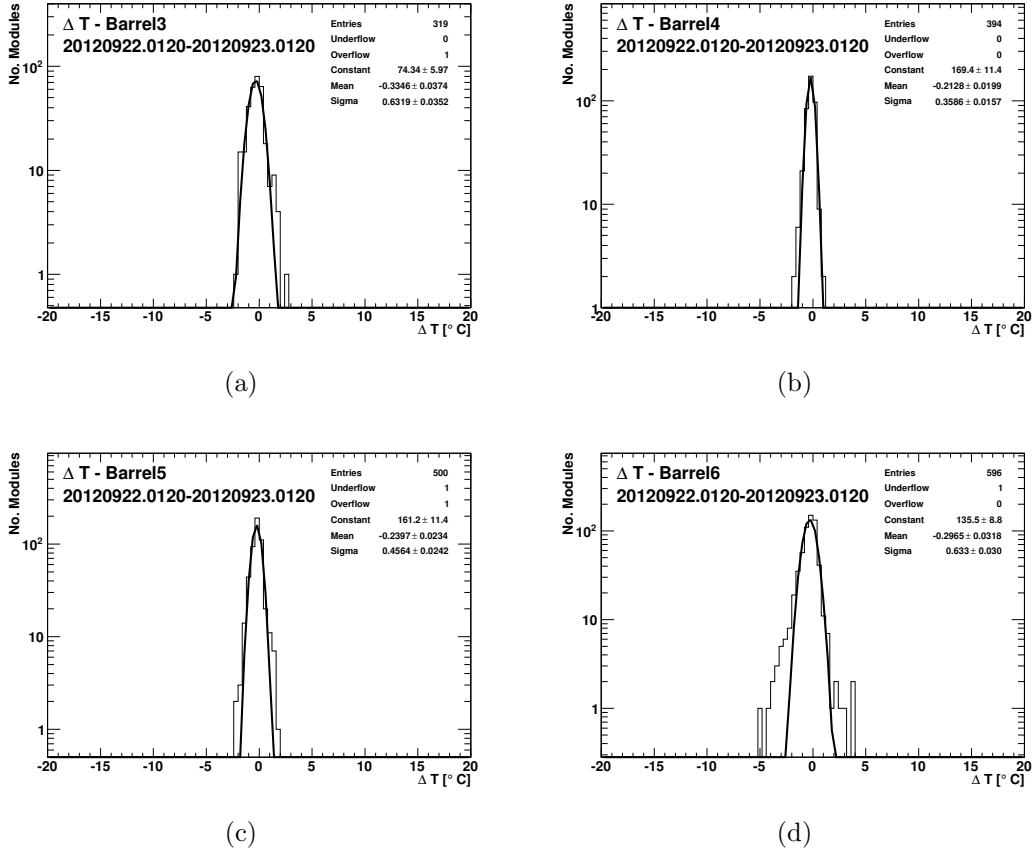


Figure 4.2:  $\Delta T$  distributions for the SCT Barrel 3 (a), Barrel 4 (b), Barrel 5 (c) and Barrel 6 (d) for 01:20 22/9/2012 to 01:20 23/9/2012. The distributions are fit to a Gaussian; the mean and width of the Gaussian is indicated on the plot.

greater than the threshold are identified as ‘problem modules’. Table 4.2 gives the number and percentage of modules with front-back temperature difference greater than the threshold at least five times during the period 20/1/2010 - 19/6/2010 for each barrel layer. The width of the distribution is greatest for Barrel 3, and so the thresholds for identifying high  $\Delta T$  modules is highest for this barrel. The width of the distribution for Barrel 6 is the second widest, however the distribution is observed to have large non Gaussian tails. Subsequently, the percentage of modules falling outside of the Gaussian is far higher than for other barrels and so a higher

Barrel	$\sqrt{\langle \sigma^2 \rangle}$	$5\sqrt{\langle \sigma^2 \rangle}$	$\chi^2 / \text{ndf}$	$\langle \Delta T_{\text{mean}} \rangle$
All barrels	0.52	2.61	132.64	-0.25
Barrel 3	0.64	3.21	19.44	-0.36
Barrel 4	0.39	1.96	8.22	-0.21
Barrel 5	0.48	2.38	36.06	-0.23
Barrel 6	0.60	3.02	59.06	-0.26

Table 4.1: The width, goodness of fit and mean of the Gaussian fit to the  $\Delta T$  distribution averaged over stable periods between 20/1/2010 and 20/6/2010.

portion of the modules on Barrel 6 are identified as problematic than on other barrels. This is explained by the fact that for Barrels 3, 4 and 5 only modules with  $|\Delta T| < 2^\circ\text{C}$  measured on production were accepted, whereas for Barrel 6 this was relaxed to  $|\Delta T| < 4^\circ\text{C}$  [10].

The mean value of the  $\Delta T$  distributions tend to be negative, implying that on average the back side of the modules (the side facing into the carbon fibre barrel) tend to be warmer than the front. This effect was also observed in tests carried out on the modules reception at CERN in 2006 [10], and in tests carried out in 2008 [11]. Investigations suggested that this bias is a property of the module itself, rather than an effect due to the module's environment. A possible explanation is that the bend in the hybrid is on the back of the module, and this may have caused difficulties in manufacturing an effective glue joint, increasing thermal impedance and causing a weaker thermal coupling between the cooling pipe and the back of the module.

### 4.3.2 Module temperature variation - $T_{\text{diff}}$

Modules with a bad thermal coupling to the cooling pipe can be identified by looking for modules with a temperature significantly different to other modules

Component	# Problem Modules	% Modules Problematic
Barrel 3	1	0.3
Barrel 4	1	0.2
Barrel 5	7	1.2
Barrel 6	17	2.5

Table 4.2: Number and percentage of modules with  $|\Delta T|$  greater than the threshold for identifying problem modules at least 5 times during the period 20/1/2010 - 19/6/2010 for each barrel.

on the same cooling structure. The monitoring variable  $T_{\text{diff}}$  is defined as  $T_{\text{diff}} = \bar{T}_{\text{struct}} - T_{\text{module}}$  where  $\bar{T}_{\text{struct}} = \sum_1^N T_i/N$  is the average temperature of modules on the cooling structure. For the SCT barrels a cooling structure is defined as a stave (consisting of two loops) and for endcaps a cooling loop. Any module warmer than its neighbours gives a negative value of  $T_{\text{diff}}$  whilst modules cooler than their neighbours give a positive value.

Figure 4.3 shows the distributions of  $T_{\text{diff}}$  for the barrel and for each of the endcaps for 01:20 22/9/2012 to 01:20 23/9/2012. As expected the mean of the distribution is consistent with zero. Endcap C shows a large tail to low  $T_{\text{diff}}$ , indicating there are a large number of modules warmer than other modules on their cooling loop. Examination of the distributions for each disk suggest that this effect is observed on disks 1-5, but not on disks 6-9.

As with the  $\Delta T$  monitoring variable, five times the average width of the Gaussian fit is used as a threshold for identifying problem modules. The threshold is set separately for each SCT barrel layer and endcap disk. The thresholds are given in Table 4.3. The endcaps tend to have much wider distributions than the barrels, indicating that the module temperature is less uniform on endcap cooling loops. This is consistent with the findings of the 2008 study. The number and percentage

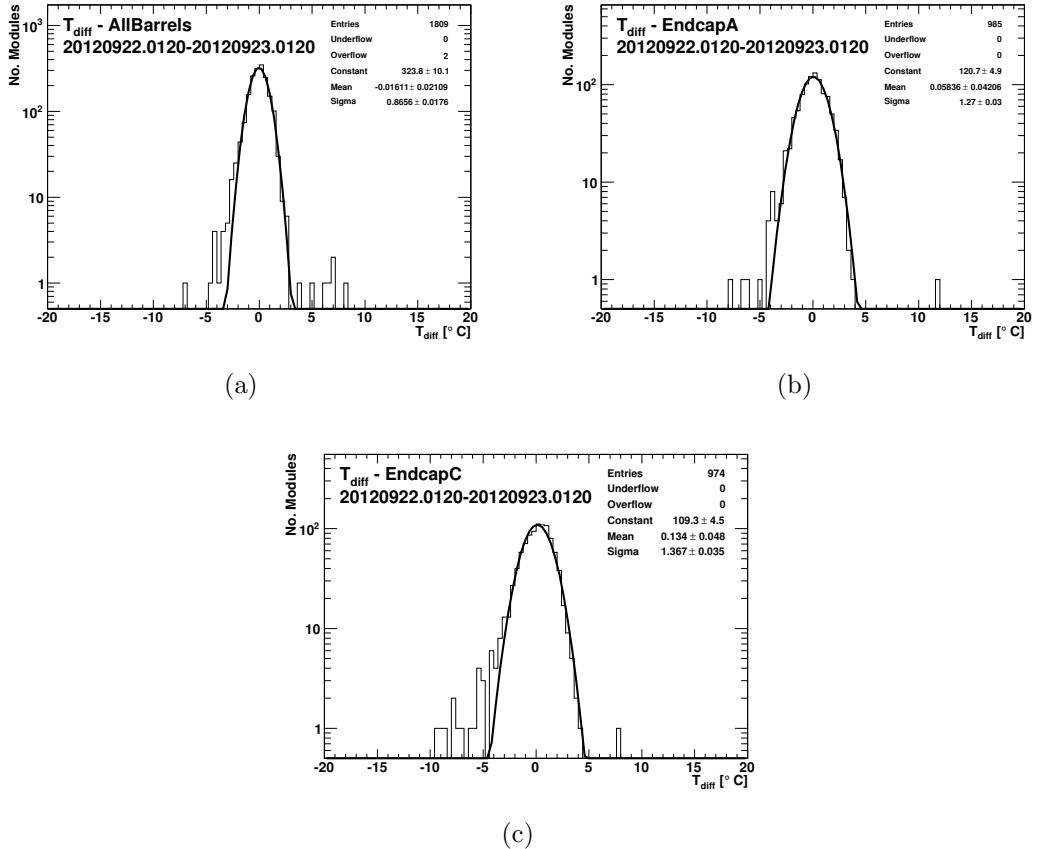


Figure 4.3:  $T_{\text{diff}}$  distributions for the SCT barrel and endcaps for 01:20 22/9/2012 to 01:20 23/9/2012

of modules with  $|T_{\text{diff}}|$  greater than threshold at least 5 times during the period 20/1/2010 - 19/6/2010 is shown in Table 4.4.

The majority of the modules above threshold had negative values of  $T_{\text{diff}}$  , indicating that they are warmer than their neighbours. This is generally caused by the modules not being in complete contact with their cooling block. A small number of modules had very large positive values of  $T_{\text{diff}}$  , indicating that they are cooler than their neighbours. This indicates a lower power dissipation through the module which is either due to the module being disabled and thus not receiving the high voltage current, or due to incorrect chip settings.

Barrel	$\sqrt{\langle \sigma^2 \rangle}$	$5\sqrt{\langle \sigma^2 \rangle}$	$\chi^2 / \text{ndf}$
<b>All Barrels</b>	0.81	4.03	48.82
Barrel3	0.87	4.33	12.66
Barrel4	0.71	3.56	13.88
Barrel5	0.82	4.09	18.5
Barrel6	0.77	3.84	35.44
<b>EndcapA All Disks</b>	1.31	6.53	28.68
EndcapA Disk1	1.33	6.67	11.17
EndcapA Disk2	1.38	6.89	14.93
EndcapA Disk3	1.26	6.31	15.21
EndcapA Disk4	1.28	6.42	11.04
EndcapA Disk5	1.49	7.43	19.32
EndcapA Disk6	1.45	7.27	15.54
EndcapA Disk7	1.81	9.05	13.96
EndcapA Disk8	1.39	6.95	10.05
EndcapA Disk9	1.96	9.8	9.05
<b>EndcapC All Disks</b>	1.31	6.57	44.63
EndcapC Disk1	1.24	6.21	17.52
EndcapC Disk2	1.41	7.03	14.18
EndcapC Disk3	1.26	6.28	19.22
EndcapC Disk4	1.41	7.07	18.36
EndcapC Disk5	1.19	5.96	19.22
EndcapC Disk6	1.64	8.22	11.29
EndcapC Disk7	1.25	6.27	11.17
EndcapC Disk8	1.29	6.47	13.39
EndcapC Disk9	1.72	8.58	9.38

Table 4.3: The rms width of a Gaussian fit to the  $T_{\text{diff}}$  distribution for each stable period between 20/1/2010 and 20/6/2010. The threshold used for identifying high  $T_{\text{diff}}$  modules is set as 5 times this value; this is also shown in the second column. The third column shows the  $\chi^2$  goodness of fit parameter.

Component	# Problem Modules	% Modules Problematic
Barrel 3	3	0.8
Barrel 4	1	0.2
Barrel 5	3	0.5
Barrel 6	6	0.9
Endcap A	4	0.4
Endcap C	9	0.9

Table 4.4: Number and percentage of modules with  $|T_{\text{diff}}|$  greater than the threshold for identifying problem modules at least 5 times during the period 20/1/2010 - 19/6/2010 for each barrel and for each of the endcaps.

## 4.4 Time Evolution of monitoring variables

In order to track problematic modules, plots are produced each month showing the problem modules and on which days they were problematic. An example of such a plot is shown in Figure 4.4. These plots are available on the Calibration Monitoring website.

### 4.4.1 Number of Problem modules

Of obvious concern is whether the number of problematic modules is increasing. Figure 4.5 shows the number of problem modules above threshold on a given day as a function of time between 20/01/2010 to 16/10/2012 for the  $\Delta T$  and  $T_{\text{diff}}$  monitoring variables. For both monitoring variables, there is no significant increase in the number of problematic variables observed as a function of time. Fitting the distributions to a linear function, the average number of  $T_{\text{diff}}$  modules above the problem threshold is found to increase at a rate of  $0.74 \pm 0.05$  per year. The average number of  $\Delta T$  modules above the problem threshold is found to increase at a rate of  $2.54 \pm 0.15$  per year.

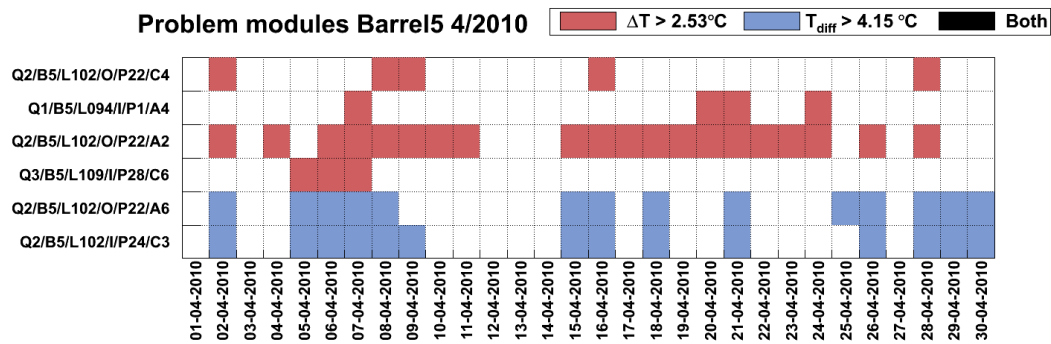


Figure 4.4: Problem modules on barrel 5 in April 2010

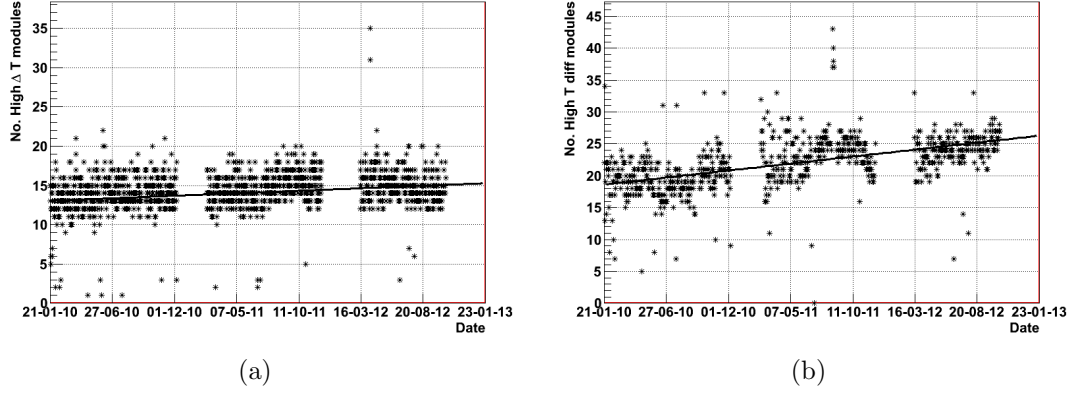


Figure 4.5: The number of ‘problematic’ modules with (a)  $\Delta T$  and (b)  $T_{\text{diff}}$  of greater magnitude than the problem threshold per day as a function of time between 20/01/2010 to 16/10/2012. The number of ‘problematic’ modules is not seen to increase significantly as a function of time.

## 4.5 Behaviour of problematic modules

For each of the problematic modules the value of the problematic monitoring variable has been plotted as a function of time for the first six months of 2010 in order to determine whether the problem is getting worse. For most of the problematic modules the magnitude of the monitoring variable does not increase over the period, aside from small fluctuations. However, one module has been identified with a high  $\Delta T$  of increasing magnitude, and four modules with a  $T_{\text{diff}}$  of increasing magnitude. A further two show odd behavior.

The plot on the left of 4.6 shows the only module with a  $\Delta T$  of increasing magnitude. The temperature difference between the front and back of the module has increased by about  $1.5^{\circ}\text{C}$  in six months, with back of the module warmer than the front. This suggests that the two sides of the module are slowly separating. The plot on the right of 4.6 shows a module for which  $\Delta T$  jumps between  $0^{\circ}\text{C}$  and  $3\text{-}4^{\circ}\text{C}$  every 1 or 2 months. This suggests an intermittent failure in the integrity of

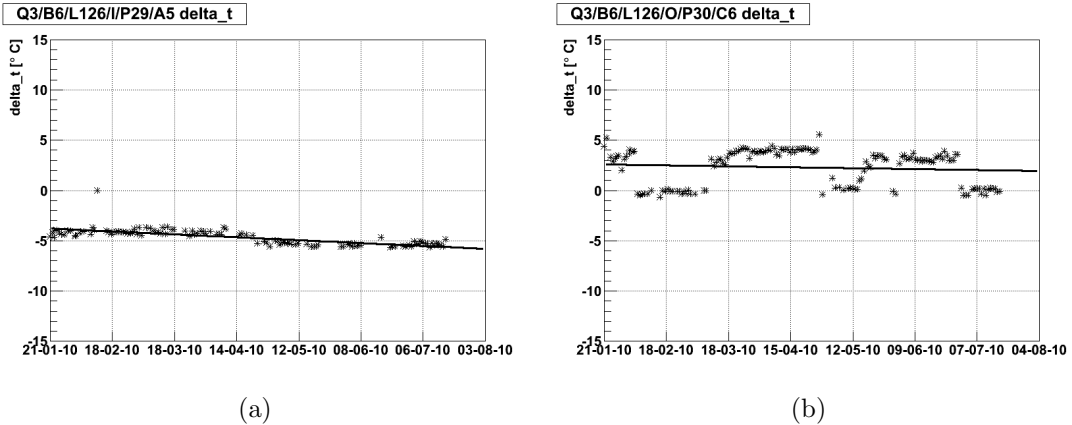


Figure 4.6: The temperature difference between the front and back of the module ( $\Delta T$ ) for barrel module Q3/B6/L126/I/P29/A5 (left) and barrel module Q3/B6/L126/O/P30/C6 (right) as a function of time between 20/1/2010 to 18/7/2010

the module, but is very unexpected behaviour and requires further investigation.  
No other problems with this module have been recorded.

Three modules were observed to have a  $T_{\text{diff}}$  becoming more negative with time, indicating that they are becoming warmer relative to their neighbours by about 1°C over six months. This suggests a failure in coupling to the cooling pipe that is getting worse with time. One of these modules is shown on the left of Figure 4.7. The right hand plot of Figure 4.7 shows a module with  $T_{\text{diff}}$  becoming more positive over time, and also showing sharp jumps in the variable. An increasing positive  $T_{\text{diff}}$  means the module is cooler than its neighbours, and becoming even more cooler. This would suggest that the module is running at a lower power, although it is unclear why this would cause the  $T_{\text{diff}}$  to increase over time, nor explain the sudden jumps. Generally modules running at lower power are detected with the DAQ (Data Acquisition) software, but no problem has been reported for this module. A further seven modules with a  $T_{\text{diff}}$  which jumps between 0°C and around

$+7^{\circ}\text{C}$  have been observed. All seven of these modules have other known problems; either the modules do not receive the high voltage, or there is a problem with the module communication. These modules are out of configuration, and data sent from these modules is not used for physics.

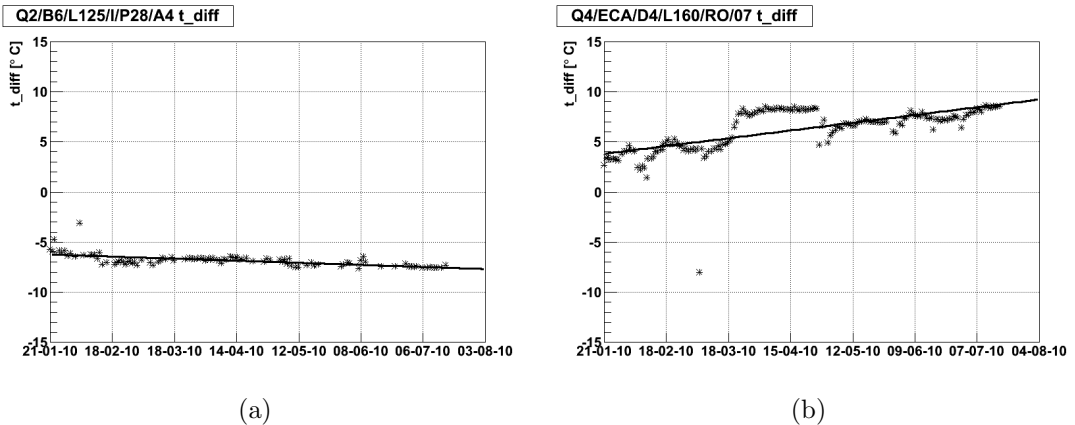


Figure 4.7: The difference in temperature between the module and its neighbours ( $T_{\text{diff}}$ ) as a function of time for module Q2/B5/L102/I/P24/C3 (left) Q4/ECA/D4/L160/RO/07 (right) between 20/1/2010 to 18/7/2010.

## 4.6 Conclusions

I plan to cross check problem modules against detector conditions and coincidences with events like power-cuts, shutdowns, cooling failures etc, as well as studying characteristics of the individual modules such as the voltage arriving at the module. I also plan to cross check problematic modules against the ‘production database’ which details tests made of modules at production to identify any correlations.

# **Chapter 5**

## **Object Reconstruction**

## **Part III**

## **Analysis**

# **Chapter 6**

## **Object and Event Selection**

Describe and motivate electron / muon / jet selection requirements. Describe and motivate event selection. Give details of mis-pairing rate, contamination from taus and events outside fiducial volume, etc. Show observed kinematic distributions.

# **Chapter 7**

## **Background Estimate**

Describe data and MC background estimates Show control plots

# **Chapter 8**

## **CrossSection**

**8.1 Cross Section Definition**

**8.2 Acceptances**

**8.3 Systematic Uncertainties**

**8.4 Cross Section Extraction**

# **Chapter 9**

## **TGCLimits**

# **Chapter 10**

## **Exotics**

# **Chapter 11**

## **Conclusions**

# Bibliography

- [1] J.-L. Caron, *ATLAS detector in A4 format with English captions.*, AC Collection. Legacy of AC. Pictures from 1992 to 2002., Mar, 1998.
- [2] ATLAS Collaboration, *Expected performance of the ATLAS experiment: detector, trigger and physics.* CERN, Geneva, 2009.
- [3] A. Collaboration, *The ATLAS Experiment at the CERN Large Hadron Collider*, Journal of Instrumentation **3** (2008) no. 08, S08003.  
<http://stacks.iop.org/1748-0221/3/i=08/a=S08003>.
- [4] O. S. Brning, P. Collier, P. Lebrun, S. Myers, R. Ostojic, J. Poole, and P. Proudlock, *LHC Design Report.* CERN, Geneva, 2004.
- [5] *LHC Performance and Statistics*,  
<https://lhc-statistics.web.cern.ch/LHC-Statistics/>.
- [6] D. Fournier, *Performance of the LHC, ATLAS and CMS in 2011*, EPJ Web Conf. **28** (2012) 01003, [arXiv:1201.4681 \[hep-ex\]](https://arxiv.org/abs/1201.4681).
- [7] A. Ahmad, Z. Albrechtskirchinger, P. Allport, J. Alonso, L. Andricek, R. Apsimon, A. Barr, R. Bates, G. Beck, P. Bell, A. Belymam, J. Benes, C. Berg, J. Bernabeu, S. Bethke, N. Bingefors, J. Bizzell, J. Bohm,

R. Brenner, T. Brodbeck, P. B. D. Renstrom, C. Buttar, D. Campbell,  
C. Carpentieri, A. Carter, J. Carter, D. Charlton, G.-L. Casse,  
A. Chilingarov, V. Cindro, A. Ciocio, J. Civera, A. Clark, A.-P. Colijn,  
M. Costa, W. Dabrowski, K. Danielsen, I. Dawson, B. Demirkoz, P. Dervan,  
Z. Dolezal, O. Dorholt, I. Duerdoth, M. Dwuznik, S. Eckert, T. Ekelf,  
L. Eklund, C. Escobar, D. Fasching, L. Feld, D. Ferguson, D. Ferrere,  
R. Fortin, J. Foster, H. Fox, R. French, B. Fromant, K. Fujita, J. Fuster,  
S. Gadomski, B. Gallop, C. Garca, J. Garca-Navarro, M. Gibson,  
S. Gonzalez, S. Gonzalez-Sevilla, M. Goodrick, E. Gornicki, C. Green,  
A. Greenall, C. Grigson, A. Grillo, J. Grosse-Knetter, C. Haber, T. Handa,  
K. Hara, R. Harper, F. Hartjes, T. Hashizaki, D. Hauff, N. Hessey, J. Hill,  
T. Hollins, S. Holt, T. Horazdovsky, M. Hornung, K. Hovland, G. Hughes,  
T. Huse, Y. Ikegami, Y. Iwata, J. Jackson, K. Jakobs, R. Jared,  
L. Johansen, R. Jones, T. Jones, P. de Jong, J. Joseph, P. Jovanovic,  
J. Kaplon, Y. Kato, C. Ketterer, I. Kindervaag, P. Kodys, E. Koffeman,  
T. Kohriki, Z. Kohout, T. Kondo, S. Koperny, E. van der Kraaij, V. Kral,  
G. Kramberger, J. Kudlaty, C. Lacasta, M. Limper, V. Linhart, G. Llos,  
M. Lozano, I. Ludwig, J. Ludwig, G. Lutz, A. Macpherson, S. McMahon,  
D. Macina, C. Magrath, P. Malecki, I. Mandi, S. Mart-Garca, T. Matsuo,  
J. Meinhardt, B. Mellado, I. Mercer, M. Mikestikova, M. Miku, M. Miano,  
J. Mistry, V. Mitsou, P. Modesto, B. Mohn, S. Molloy, G. Moorhead,  
A. Moraes, D. Morgan, M. Morone, J. Morris, H.-G. Moser, A. Moszczynski,  
A. Muijs, K. Nagai, Y. Nakamura, I. Nakano, R. Nicholson, T. Niinikoski,  
R. Nisius, T. Ohsugi, V. OShea, O. Oye, U. Parzefall, J. Pater,  
H. Pernegger, P. Phillips, S. Pospisil, P. Ratoff, P. Reznicek, J. Richardson,

R. Richter, D. Robinson, S. Roe, G. Ruggiero, K. Runge, H. Sadrozinski,  
H. Sandaker, J. Schieck, A. Seiden, S. Shinma, J. Siegrist, T. Sloan,  
N. Smith, S. Snow, M. Solar, A. Solberg, B. Sopko, L. Sospedra, H. Spieler,  
E. Stanecka, S. Stapnes, J. Stastny, F. Stelzer, A. Stradling, B. Stugu,  
R. Takashima, R. Tanaka, G. Taylor, S. Terada, R. Thompson, M. Titov,  
Y. Tomeda, D. Tovey, M. Turala, P. Turner, M. Tyndel, M. Ulln, Y. Unno,  
T. Vickey, M. Vos, R. Wallny, P. Weilhammer, P. Wells, J. Wilson,  
M. Wolter, M. Wormald, S. Wu, T. Yamashita, D. ontar, and A. Zsenei, *The  
silicon microstrip sensors of the ATLAS semiconductor tracker*, Nuclear  
Instruments and Methods in Physics Research Section A: Accelerators,  
Spectrometers, Detectors and Associated Equipment **578** (2007) no. 1, 98 –  
118. <http://www.sciencedirect.com/science/article/pii/S0168900207007644>.

- [8] G. Lindstrm, M. Ahmed, S. Albergo, P. Allport, D. Anderson, L. Andricek,  
M. Angarano, V. Augelli, N. Bacchetta, P. Bartalini, R. Bates, U. Biggeri,  
G. Bilei, D. Bisello, D. Boemi, E. Borchi, T. Botila, T. Brodbeck, M. Bruzzi,  
T. Budzynski, P. Burger, F. Campabadal, G. Casse, E. Catacchini,  
A. Chilingarov, P. Ciampolini, V. Cindro, M. Costa, D. Creanza, P. Clauws,  
C. D. Via, G. Davies, W. D. Boer, R. DellOrso, M. D. Palma, B. Dezillie,  
V. Eremin, O. Evrard, G. Fallica, G. Fanourakis, H. Feick, E. Focardi,  
L. Fonseca, E. Fretwurst, J. Fuster, K. Gabathuler, M. Glaser, P. Grabiec,  
E. Grigoriev, G. Hall, M. Hanlon, F. Hauler, S. Heising, A. Holmes-Siedle,  
R. Horisberger, G. Hughes, M. Huhtinen, I. Ilyashenko, A. Ivanov, B. Jones,  
L. Jungermann, A. Kaminsky, Z. Kohout, G. Kramberger, M. Kuhnke,

S. Kwan, F. Lemeilleur, C. Leroy, M. Letheren, Z. Li, T. Ligonzio,  
 V. Linhart, P. Litovchenko, D. Loukas, M. Lozano, Z. Luczynski, G. Lutz,  
 B. MacEvoy, S. Manolopoulos, A. Markou, C. Martinez, A. Messineo,  
 M. Miku, M. Moll, E. Nossalzewska, G. Ottaviani, V. Oshea, G. Parrini,  
 D. Passeri, D. Petre, A. Pickford, I. Pintilie, L. Pintilie, S. Pospisil,  
 R. Potenza, C. Raine, J. Rafi, P. Ratoff, R. Richter, P. Riedler, S. Roe,  
 P. Roy, A. Ruzin, A. Ryazanov, A. Santocchia, L. Schiavulli, P. Sicho,  
 I. Siotis, T. Sloan, W. Slysz, K. Smith, M. Solanky, B. Sopko, K. Stolze,  
 B. S. Avset, B. Svensson, C. Tivarus, G. Tonelli, A. Tricomi, S. Tzamarias,  
 G. Valvo, A. Vasilescu, A. Vayaki, E. Verbitskaya, P. Verdini, V. Vrba,  
 S. Watts, E. Weber, M. Wegrzecki, I. Wegrzecka, P. Weilhammer,  
 R. Whealon, C. Wilburn, I. Wilhelm, R. Wunstorf, J. Wstenfeld, J. Wyss,  
 K. Zankel, P. Zabierowski, and D. ontar, *Radiation hard silicon  
 detectorsdevelopments by the RD48 (ROSE) collaboration*, Nuclear  
 Instruments and Methods in Physics Research Section A: Accelerators,  
 Spectrometers, Detectors and Associated Equipment **466** (2001) no. 2, 308 –  
 326. <http://www.sciencedirect.com/science/article/pii/S0168900201005605>.  
 jce:title}4th Int. Symp. on Development and Application of Semiconductor  
 Tracking Detectorsj/ce:title}.

- [9] D. Attree, B. Anderson, E. C. Anderssen, V. Akhnazarov, R. J. Apsimon,  
 P. Barclay, L. E. Batchelor, R. L. Bates, M. Battistin, J. Bendotti, S. Berry,  
 A. Bitadze, J. P. Bizzel, P. Bonneau, M. Bosteels, J. M. Butterworth,  
 S. Butterworth, A. A. Carter, J. R. Carter, A. Catinaccio, F. Corbaz, H. O.

Danielsson, E. Danilevich, N. Dixon, S. D. Dixon, F. Doherty, O. Dorholt,  
M. Doubrava, K. Egorov, K. Einsweiler, A. C. Falou, P. Feraudet, P. Ferrari,  
K. Fowler, J. T. Fraser, R. S. French, M. Galuska, F. Gannaway,  
G. Gariano, M. D. Gibson, M. Gilchriese, D. Giugni, J. Godlewski,  
I. Gousakov, B. Gorski, G. D. Hallewell, N. Hartman, R. J. Hawkings, S. J.  
Haywood, N. P. Hessey, I. Ilyashenko, S. Infante, J. N. Jackson, T. J. Jones,  
J. Kaplon, S. Katunin, S. Lindsay, L. Luisa, N. Massol, F. McEwan, S. J.  
McMahon, C. Menot, J. Mistry, J. Morris, D. M. Muskett, K. Nagai,  
A. Nichols, R. Nicholson, R. B. Nickerson, S. L. Nielsen, P. E. Nordahl,  
M. Olcese, M. Parodi, F. Perez-Gomez, H. Pernegger, E. Perrin, L. P. Rossi,  
A. Rovani, E. Ruscino, H. Sandaker, A. Smith, V. Sopko, S. Stapnes,  
M. Stodulski, J. Tarrant, J. Thadome, D. Tovey, M. Turala, M. Tyndel,  
V. Vacek, E. van der Kraaij, G. H. A. Viehhauser, E. Vigeolas, P. S. Wells,  
S. Wenig, and P. Werneke, *The evaporative cooling system for the ATLAS  
inner detector*, Journal of Instrumentation **3** (2008) no. 07, P07003.  
<http://stacks.iop.org/1748-0221/3/i=07/a=P07003>.

- [10] ATLAS Collaboration, G. Viehhauser, B. Mikulec, A. Sfyrla, and A. Robichaud-Veronneau, *Temperature behaviour and uniformity of SCT barrels during assembly and reception testing*, . ATL-INDET-PUB-2006-009.
- [11] K. Shaw and S. D'Auria, *SCT Cooling and Environment 2008 Performance: SCT Cooling and Environment 2008 Performance*, ATL-COM-INDET-2009-094, Dec, 2009.